

# **Anomalous Hall and Nernst effects in ferrimagnetic Mn<sub>4</sub>N films: possible interpretation and prospect for enhancement**

Shinji Isogami<sup>1\*</sup>, Keisuke Masuda<sup>1</sup>, Yoshio Miura<sup>1</sup>, Rajamanickam Nagalingam<sup>1</sup>, and Yuya Sakuraba<sup>1,2</sup>

<sup>1</sup> Research Center for Magnetic and Spintronic Materials, National Institute for Materials Science, Sengen 1-2-1, Tsukuba, Ibaraki, 305-0047 Japan

<sup>2</sup> PRESTO, Japan Science and technology Agency, Saitama 332-0012, Japan

\*E-mail: isogami.shinji@nims.go.jp

**Ferrimagnetic Mn<sub>4</sub>N is a promising material for heat flux sensors based on the anomalous Nernst effect (ANE) because of its sizable uniaxial magnetic anisotropy ( $K_u$ ) and low saturation magnetization ( $M_s$ ). We experimentally and theoretically investigated the ANE and anomalous Hall effect in sputter-deposited Mn<sub>4</sub>N films. It was revealed that the observed negative anomalous Hall conductivity ( $\sigma_{xy}$ ) could be explained by two different coexisting magnetic structures, that is, a dominant magnetic structure with high  $K_u$  contaminated by another structure with negligible  $K_u$  owing to an imperfect degree of order of nitrogen. The observed transverse thermoelectric power ( $S_{ANE}$ ) of +0.5  $\mu\text{V/K}$  at 300 K gave a transverse thermoelectric**

coefficient ( $\alpha_{xy}$ ) of +0.34 A/(m·K), which was smaller than the value predicted from first-principles calculation. The interpretation for  $\alpha_{xy}$  based on the first-principles calculations led us to conclude that the realization of single magnetic structure with high  $K_u$  and optimal adjustment of the Fermi level are promising approaches to enhance  $S_{ANE}$  in Mn<sub>4</sub>N through the sign reversal of  $\sigma_{xy}$  and the enlargement of  $\alpha_{xy}$  up to a theoretical value of 1.77 A/(m·K).

#### <Main text>

Thermoelectric conversion based on the anomalous Nernst effect (ANE)<sup>1)</sup> is an intriguing alternative technology to those based on the conventional Seebeck effect,<sup>2)</sup> because the transverse thermoelectric power based on the ANE ( $S_{ANE}$ ) is given in the perpendicular direction with respect to the heat current as shown in the following equation,

$$\mathbf{E}_{ANE} = S_{ANE} \nabla T \times \left( \frac{\mathbf{M}}{|\mathbf{M}|} \right), \quad (1)$$

where  $\mathbf{E}_{ANE}$ ,  $\mathbf{M}$ , and  $\nabla T$  denote the electric field due to the ANE, magnetization, and temperature gradient, respectively. Owing to these characteristics, a prototype coplanar-type thermopile module has been fabricated using magnetic materials and an enhancement of the serial voltage has been demonstrated.<sup>3,4)</sup>

One of the most promising applications of the ANE-based coplanar thermopile structure is heat flux sensors. Zhou *et al.* recently fabricated a prototype ANE-based heat flux sensor on a flexible thin polyimide sheet and successfully demonstrated heat flux sensing through ANE.<sup>5)</sup>

Although the sensor has the potential to be versatile because of its high flexibility and low thermal resistance, its low sensitivity is the most important issue to be solved. To overcome this problem, magnetic materials with large  $S_{ANE}$  are indispensable.<sup>6)</sup> Furthermore, because the magnetization direction must be aligned to the width direction of magnetic wires even at zero field, low  $M_s$  is also an important factor in decreasing the demagnetization field in magnetic wires that causes a reduction of  $E_{ANE}$  in the zero-field state.<sup>5)</sup> To stabilize the spontaneous magnetization, high uniaxial magnetic anisotropy ( $K_u$ ) is also desirable. In recent years, ferromagnetic Heusler alloys such as  $\text{Co}_2\text{MnGa}$ <sup>7-9)</sup> and  $\text{Co}_2\text{MnAl}_{0.63}\text{Si}_{0.37}$ <sup>10)</sup> have exhibited high  $S_{ANE}$  of  $\sim 6 \mu\text{V/K}$ . However, their high  $M_s$  and low  $K_u$  are not suitable for a heat flux sensor. In contrast,  $0.1\sim 0.5 \mu\text{V/K}$  was reported in  $\text{Mn}_3\text{Sn}$  films regardless of its extremely low  $M_s$  down to  $\sim 10^{-3} \text{ T}$ .<sup>11)</sup> However, its  $S_{ANE}$  value is not sufficient for the sensor. Therefore, exploring magnetic materials with high  $S_{ANE}$ , low  $M_s$ , and high  $K_u$  has been of significant importance.

As a promising candidate material with low  $M_s$  and high  $K_u$ , we focus on  $\text{Mn}_4\text{N}$  in the present study.  $\text{Mn}_4\text{N}$  film has long been known as a Mn-based perpendicular magnetic anisotropy (PMA) ferrimagnetic material with an antiperovskite structure described by the formula  $\text{ANB}_3$ , where A and B correspond to Mn(I) at corner sites and Mn(II) at face-centered sites.<sup>12,13)</sup> Owing to the ferrimagnetism of  $\text{Mn}_4\text{N}$ , the  $M_s$  is much smaller than in conventional ferromagnets such as Co-based Heusler alloys, Fe-based alloys, and nitride systems. The high  $K_u$  in  $\text{Mn}_4\text{N}$  is also an attractive feature

for usage in ANE-based thermoelectric applications. The Mn<sub>4</sub>N films fabricated by sputtering and molecular-beam epitaxy (MBE) in previous studies exhibited  $M_s \approx 0.1$  T and  $K_u \approx 0.1$  MJ/m<sup>3</sup>.<sup>14-19</sup> While the AHE for Mn<sub>4</sub>N has been reported,<sup>17,20</sup> the ANE and AHE including the analysis from the perspective of intrinsic mechanism have not been studied so far.

In this study, we measured both the ANE and AHE of Mn<sub>4</sub>N films to analyze the mechanisms of ANE. As a result, we revealed that the Mn<sub>4</sub>N is one of a few materials that satisfies the requirements of  $M_s$  and  $K_u$  for heat flux sensors while the  $S_{ANE}$  was moderate. The first-principles calculations revealed that two different magnetic structures coexist in present Mn<sub>4</sub>N films and adjustment of the Fermi level is necessary to enhance the ANE.

Two 20-nm-thick Mn<sub>4</sub>N films were grown on single-crystal MgO(001) substrates by reactive nitridation sputtering at substrate temperatures of 450 °C and 400 °C (referred to as “sample-I” and “sample-II” in this study, respectively), and 2-nm-thick Al films were then deposited as a capping layer. The flow ratio of N<sub>2</sub> to Ar gas was 12%. Structural analysis was performed using X-ray diffractometry (XRD) with Cu  $K_{\alpha}$  radiation (SmartLab: Rigaku, Inc.). Magnetic properties were measured using a superconducting quantum interference device vibrating sample magnetometer (SQUID-VSM: Quantum Design, Inc.). The  $K_u$  was estimated by  $M_s H_k/2 + M_s^2/2\mu_0$ , where the anisotropy field  $H_k$  is defined as the saturation magnetic field difference between in-plane and out-of-plane directions. The ANE and AHE were measured using a physical property measurement system

(VersaLab: Quantum Design, Inc.). Rectangular pattern samples with dimensions of  $w = 2$  mm and  $l = 7$  mm were prepared using photolithography and Ar ion milling. The anomalous Hall (Nernst) voltage  $V_{\text{AHE}}$  ( $V_{\text{ANE}}$ ) was measured in the  $y$ -direction by applying  $I_x$  ( $\nabla T_x$ ) and the external magnetic field  $H_z$  ( $H_z$ ), as shown in Fig. 1.  $\nabla T_x$  was strictly measured by an infrared camera with a black body coating on the sample.<sup>5,10,21</sup> The Seebeck coefficients of the films ( $S_{\text{SE}}$ ) were measured using a ZEM-3 (ADVANCE RIKO, Inc.) with R-type thermocouples.

In the theoretical calculation of the anomalous Hall conductivity ( $\sigma_{xy}$ ) and the transverse thermoelectric coefficient ( $\alpha_{xy}$ ), we combined the first-principles calculations and the Boltzmann transport theory. The electronic structure of the stoichiometric  $\text{Mn}_4\text{N}$  was first calculated using the full-potential linearized augmented plane-wave method including the effect of spin-orbit interactions, which was implemented in the WIEN2K program.<sup>22</sup> The lattice constants of the unit cell were fixed at  $a = 3.87726$  Å and  $c = 3.83974$  Å ( $c/a = 0.99$ ), which were the experimental values evaluated from the in-plane and out-of-plane XRD profiles. The self-consistent-field calculation using  $24 \times 24 \times 25$   $k$  points gave both type-A and -B. For the obtained electronic structures, we calculated  $\sigma_{xy}$  and  $\alpha_{xy}$  employing the same method as that used in our previous work.<sup>9</sup> In the calculation of  $\alpha_{xy}$ , the temperature  $T$  was set to 300 K. We used  $89 \times 89 \times 90$   $k$  points for the Brillouin-zone integration, ensuring good convergence for  $\sigma_{xy}$  and  $\alpha_{xy}$ .

Figures 2(a) and 2(b) show the out-of-plane XRD profiles for sample-I and -II,

respectively. The diffraction peaks at  $2\theta/\omega \approx 23^\circ$  and  $47^\circ$  correspond to the (001) superlattice and (002) fundamental peaks of Mn<sub>4</sub>N crystals, respectively. The  $S$  for sample-I (sample-II) was 0.7 (0.6), estimated based on the integral diffraction intensity of the Mn<sub>4</sub>N(001) and (002) peaks.<sup>23</sup> Figure 2(c) shows the magnetization curves for sample-I, where  $H$  was swept along the [100] and [001] directions of the Mn<sub>4</sub>N crystals. Comparing the two curves, the magnetic easy-axis was found to point in the [001] direction; that is, sample-I showed sizeable PMA ( $K_u \approx 0.13$  MJ/m<sup>3</sup>). The value of  $\mu_0 M_s$  was measured to be 100 mT, comparable to that of Mn<sub>4</sub>N films fabricated by sputtering and MBE.<sup>14-19</sup> The magnetization curves of sample-II are shown in Fig. 2(d). The two curves with  $H \parallel [100]$  and [001] showed similar magnetization process, indicating negligible PMA ( $K_u \approx 0.003$  MJ/m<sup>3</sup>) for sample-II. The value of  $\mu_0 M_s$  was slightly decreased to 90 mT. These results show that high PMA is given by high  $S$ .

From the linear response equation,  $S_{ANE}$  is given by

$$S_{ANE} = \rho_{xx} \alpha_{xy} + \rho_{xy} \alpha_{xx} , \quad (2)$$

where  $\rho_{xx(xy)}$  and  $\alpha_{xx}$  denote the longitudinal (anomalous Hall) resistivity and longitudinal thermoelectric coefficients, respectively. The second term of Eq. (2) corresponds to the contribution of the AHE to the ANE; therefore, the measurement of  $\rho_{xy}$  is necessary to study the origin of  $S_{ANE}$ . Figure 3(a) shows the  $\rho_{xy}$  curves for sample-I and -II as a function of  $H_z$  at 300 K, indicating similar hysteresis to the  $M$ - $H$  curves shown in Figs. 2(c) and 2(d). Figures 3(b) and 3(c) show the measurement

temperature ( $T$ ) dependence of  $\rho_{xy}$  and  $\rho_{xx}$ , respectively.  $\rho_{xx}$  decreased with decreasing  $T$ , suggesting metallic properties for the present two films.<sup>23)</sup> Figure 3(d) shows the  $T$  dependence of  $\sigma_{xy}$  estimated using the formula,

$$\sigma_{xy} = -\frac{\rho_{xy}}{\rho_{xy}^2 + \rho_{xx}^2} \quad . \quad (3)$$

$\sigma_{xy}$  was negative for both films:  $\sigma_{xy} \approx -80$  ( $-50$ ) S/cm at 300 K, and then  $\sigma_{xy} \approx -100$  ( $-10$ ) S/cm at 4 K for sample-I (sample-II). One can find that the sign of both  $\sigma_{xy}$  was negative for all  $T$ , and the magnitude of  $\sigma_{xy}$  increased with increasing  $S$ .

Figure 4(a) shows the  $H_z$  dependence of  $V_{ANE}$  normalized by the sample width ( $w$ ) and  $\nabla T_x$  for sample-I and -II. To evaluate  $S_{ANE}$ ,  $V_{ANE}$  was measured under different  $\nabla T_x$  and the intrinsic component of ANE was evaluated by performing a linear fitting of the curve in the high  $\mu_0 H_z$  region and taking the intercept at zero field. The inset plots the dependence of  $V_{ANE}/w$  obtained by the linear fitting on  $\nabla T_x$  for the sample-I, and the slope of least-squares fitting gave an averaged  $S_{ANE}$  of 0.50  $\mu\text{V/K}$ . The  $\alpha_{xy}$  for sample-I was estimated to be 0.34 A/(m·K) using Eq. (2) with the measured values of  $S_{ANE}$ ,  $\rho_{xx(xy)}$ , and longitudinal thermoelectric coefficient  $\alpha_{xx}$  ( $= S_{SE}/\rho_{xx}$ ). In contrast, the  $\alpha_{xy}$  for sample-II was estimated to be 0.16 A/(m·K), suggesting that high  $S$  is related to high  $\alpha_{xy}$ . Figure 4(b) shows the reported  $S_{ANE}$  for various materials plotted against  $M_s$ . Based on the analysis of the required  $\mu_0 M_s$  and  $S_{ANE}$  for an ANE-based heat flux sensor reported by Zhou *et al.*,<sup>5)</sup>  $\mu_0 M_s < 0.2$  and  $S_{ANE} > 10 \mu\text{V/K}$  are required to suppress the demagnetization field to less than 0.1 T and the sensitivity to 10

$\mu\text{V}/(\text{Wm}^{-2})$  in a  $1 \times 1 \text{ cm}^2$  size sensor with  $10 \mu\text{m}$  height and the width of the magnetic wires.

Therefore, this required range is highlighted in Fig. 4(b). Although the observed  $S_{\text{ANE}}$  for sample-I [marked as a star symbol in Fig. 4(b)] does not reach the target region showing the necessary values for heat flux sensors, one can notice that  $\text{Mn}_4\text{N}$  is one of a few materials with small  $M_s$  that satisfies this target and shows a relatively high  $S_{\text{ANE}}$  value, compared to other materials such as  $\text{Mn}_3\text{Sn}^{11})$  and  $\text{D}0_{22}\text{-Mn}_3\text{Ga}^{24})$ .

The first-principles calculations for  $\sigma_{xy}$  and  $\alpha_{xy}$  were carried out from the perspective of intrinsic mechanism to understand the origin of observed AHE and ANE in  $\text{Mn}_4\text{N}$  films. Two possible collinear magnetic structures for  $\text{Mn}_4\text{N}$  were investigated in our previous study (see Fig. 1 for the magnetic structures): “type-A,” in which the magnetic moments of Mn(I) and Mn(II) point in opposite directions, giving tiny  $M_s$  ( $\approx 7.9 \text{ mT}$ ) and negligible  $K_u$ ; and “type-B,” in which the magnetic moments couple in parallel within the  $ab$ -plane and alternate along the  $c$ -direction, giving low  $M_s$  ( $\approx 0.18 \text{ T}$ ) and high  $K_u$  ( $\approx 4 \text{ MJ/m}^3$ ).<sup>19)</sup> Type-B is energetically more stable compared with type-A when  $S = 1$ .<sup>19)</sup> Because  $\mu_0 M_s$  was measured to be  $100 \text{ mT}$  and clear PMA ( $K_u \approx 0.13 \text{ MJ/m}^3$ ) was observed, we inferred that the type-B dominates the magnetic structure for sample-I. Therefore, first, the calculation of  $\sigma_{xy}$  with type-B was carried out [solid line in Fig. 5(a)]. It was revealed that the calculated  $\sigma_{xy}$  of  $573 \text{ S/cm}$  at the Fermi level ( $\mu = 0 \text{ eV}$ ) was inconsistent with the experimental value of  $-100 \text{ S/cm}$  at  $4 \text{ K}$ . Such a large discrepancy motivated us to calculate  $\sigma_{xy}$  with type-A [dashed line in Fig. 5(a)]. As a result, we

found a negative sign at the Fermi level ( $\sigma_{xy} = -500$  S/cm), which agreed with the sign of the experimental value, although the magnitude of  $\sigma_{xy}$  still showed a discrepancy. These results imply that the main magnetic structure for sample-I is type-B but contaminated by a certain amount of type-A, the contribution of which to AHE is large enough to reverse the sign of  $\sigma_{xy}$  to negative in sample-I. Although the cause of contamination of type-A is not fully understood, imperfect  $S$  should be considered. Our previous investigation revealed that  $S = 1$  can contribute to forming type-B rather than type-A due to the energetic stability of the magnetic structure.<sup>19)</sup> We thus infer that type-A, a second stable magnetic structure, possibly appears when  $S$  deviates from 1. In contrast to our samples, Kabara *et al.* measured positive  $\sigma_{xy}$  at 4 K for 100-nm-thick Mn<sub>4</sub>N films, the sign of which agreed with that for type-B.<sup>25)</sup> Such a consistency can be attributed to the enhanced  $S$  ( $\approx 0.85$ ) due to the large layer thickness,<sup>17)</sup> and the contribution from type-A, if any, might be vailed by that from type-B. As for the experimental results found in Figs. 2(c) and 2(d), the  $M_s$  and  $K_u$  for sample-II ( $S = 0.6$ ) were smaller than those for sample-I ( $S = 0.7$ ), which could be related to the higher contamination of type-A due to the lower  $S$  for sample-II. On the other hand, the negatively smaller  $\sigma_{xy}$  for sample-II compared with sample-I cannot be explained by the higher contamination of type-A, because type-A contributes to decrease the entire  $\sigma_{xy}$ . We can see a steep change in the calculated  $\sigma_{xy}$  around the Fermi level in both type-A and -B, suggesting that  $\sigma_{xy}$  was sensitive to  $\mu$  [Fig. 5(a)]. For example, the change in  $\mu$  with  $\pm 0.05$  eV provides large variation width of  $\sim 400$  S/cm for both magnetic structures. Therefore, the

shift of the Fermi level depending on  $S$  can be another cause of the negatively smaller  $\sigma_{xy}$  for sample-II compared with sample-I.

Figure 5(b) shows the  $\mu$  dependence of  $\alpha_{xy}$ , where  $T$  was set to 300 K. At the Fermi level  $\mu = 0$ ,  $\alpha_{xy}$  was 1.66 (1.77) A/(m·K) for type-A (type-B). Compared with  $|\alpha_{xy}|$  for the representative materials: 4 for  $\text{Co}_2\text{MnGa}$ ,<sup>7)</sup> 1.2 for  $\text{FeGa}$ ,<sup>21)</sup> 1.1 for  $\text{MnSi}$ ,<sup>26)</sup> 0.6 for  $\text{SrRuO}_3$ ,<sup>27)</sup> and 0.3 for  $\text{Mn}_3\text{Sn}$ <sup>11)</sup> from the experiments, and 0.9 for  $\text{FePt}$ ,<sup>28)</sup> 0.52 for  $\text{Co}$ ,<sup>28)</sup> and 0.21 for  $\text{Fe}$ <sup>28)</sup> from the calculations [all in units of A/(m·K)], one can find that the calculated  $\alpha_{xy}$  for  $\text{Mn}_4\text{N}$  based on intrinsic origins is sufficiently high in value. Therefore,  $\text{Mn}_4\text{N}$  can be a promising material for ANE. Unlike  $\sigma_{xy}$ , high  $\alpha_{xy}$  with a positive sign was predicted for both magnetic structures, which is beneficial to the enhancement of  $S_{\text{ANE}}$  even in the case of type-A contamination. However, the measured  $\alpha_{xy}$  was one order of magnitude smaller than that from the calculation. One possible explanation is the shift of Fermi level from the theoretically obtained value as well as its effect on  $\sigma_{xy}$ , because the peak around the Fermi level was remarkably sharp [Fig. 5(b)]. For example, the even small change in  $\mu$  with  $\pm 0.05$  eV provides a large variation width of  $\sim 2.7$  ( $\sim 1.8$ ) A/(m·K) for type-A (type-B). As another reason for the discrepancy, quantifying the extrinsic contributions such as skew-scattering and/or side-jump might be necessary,<sup>29)</sup> although the  $\sigma_{xx} \approx 5 \times 10^3$  ( $\Omega \text{ cm}$ )<sup>-1</sup> for sample-I and -II are categorized into the intrinsic regime based on the  $\sigma_{xy}$ – $\sigma_{xx}$  relationship.<sup>30)</sup>

We next address how to boost the ANE in  $\text{Mn}_4\text{N}$ . Equation (2) states that  $S_{\text{ANE}}$  decreases

and increases when the signs of the first ( $\rho_{xx}\alpha_{xy}$ ) and second ( $\rho_{xy}\alpha_{xx}$ ) terms are opposite and the same, respectively. In the case of the present Mn<sub>4</sub>N films, as shown in Table I, the resultant  $S_{ANE}$  lost due to  $\rho_{xy}\alpha_{xx}$  has a negative sign. In addition, the enhanced  $\alpha_{xy}$  via modulation of the Fermi level is also necessary to boost  $S_{ANE}$  for a Mn<sub>4</sub>N system. To modulate the Fermi level and obtain positive  $\rho_{xy}\alpha_{xx}$ , realizing Mn<sub>4</sub>N with ideal type-B and no/little contamination from type-A via improved  $S$  is a promising approach. Furthermore, the substitution of a third element such as Ni into Mn<sub>4</sub>N might be another interesting approach not only for enhancing  $S_{ANE}$  but also for reducing  $M_s$ .<sup>31)</sup> Therefore, the present study could open a pathway of material development for heat flux sensors on the basis of Mn<sub>4</sub>N systems.

**Table I.** Summary of coefficients related to the ANE and AHE for Mn<sub>4</sub>N.

	Experiment		Calculation	
	Sample-I	Sample-II	Type-A	Type-B
$\mu_0 M_s$ (mT)	100	88	7.9 (0 K) <sup>19)</sup>	180 (0 K) <sup>19)</sup>
$K_u$ (MJ/m <sup>3</sup> )	0.13	0.003	~0 (0 K)	4 (0 K)
$\rho_{xx}$ ( $\mu\Omega$ cm)	190	240		
$\rho_{xy}$ ( $\mu\Omega$ cm)	2.8	2.6		
$\sigma_{xy}$ (S/cm)	−80 −100 (4 K)	−50 −10 (4 K)	−573 (0 K)	500 (0 K)

$\theta_{\text{AHE}} (\%)$	1.5	1.1		
$S_{\text{SE}} (\mu\text{V/K})$	-9.7	-14		
$S_{\text{AHE}} = S_{\text{SE}} \tan \theta_{\text{AHE}}$ ( $\mu\text{V/K}$ )	-0.15	-0.15		
$\alpha_{xx} [\text{A}/(\text{m}\cdot\text{K})]$	-5.1	-5.7		
$\alpha_{xy} [\text{A}/(\text{m}\cdot\text{K})]$	0.34	0.16	1.77	1.66
$\rho_{xy} \alpha_{xy} (\mu\text{V/K})$	0.65	0.38		
$\rho_{xy} \alpha_{xx} (\mu\text{V/K})$	-0.15	-0.15		
$S_{\text{ANE}} (\mu\text{V/K})$	0.50	0.23		

In summary, we studied the AHE and ANE for sputter-deposited 20-nm-thick ferrimagnetic Mn<sub>4</sub>N films.  $S_{\text{ANE}}$  was measured to be 0.50  $\mu\text{V/K}$  at maximum at 300 K, demonstrating that Mn<sub>4</sub>N is one of a few materials that shows relatively large  $S_{\text{ANE}}$  with low  $M_s$  and high  $K_u$ . The characteristics revealed via first-principles calculation in the current Mn<sub>4</sub>N films are: i) the possible magnetic structure might be type-B, but type-A with tiny  $M_s$  and negligible  $K_u$  might be partly included; ii)  $S_{\text{ANE}}$  decreased because of the imperfect  $S$  causing the reduction of  $\alpha_{xy}$  and the negative sign of the AHE component. To reach the target of heat flux sensors, further enhancement of  $S_{\text{ANE}}$  of Mn<sub>4</sub>N is critical. Useful approaches to be considered are to obtain positive  $\sigma_{xy}$  and enhanced  $\alpha_{xy}$  via the Fermi-level tuning and improvement of  $S$  leading to type-B magnetic structure. The present study thus

provides insight into the fundamentals of transverse transport properties for Mn-based nitride systems.

### **<Acknowledgement>**

This work was supported by JSPS KANENHI Grant Nos. 19K04499, 19K21954, 18H03787, 16H06332, and PRESTO from the Japan Science and Technology Agency (No. JPMJPR17R5) and NEDO “Mitou challenge 2050” (Grant No. P14004). The authors thank B. Masaoka for his technical support. Part of this work was carried out under the Cooperative Research Project Program of the RIEC, Tohoku University.

## <References>

- [1] W. Nernst, Ann. Phys. **267**, 760 (1887).
- [2] H. J. Goldsmid, Proc. Phys. Soc. **71**, 633 (1958).
- [3] Y. Sakuraba, K. Hasegawa, M. Mizuguchi, T. Kubota, S. Mizukami, T. Miyazaki, and K. Takanashi, Appl. Phys. Express **6**, 033003 (2013).
- [4] Y. Sakuraba, Scr. Mater. **111**, 29 (2016).
- [5] W. Zhou and Y. Sakuraba, Appl. Phys. Express **13**, 043001 (2020).
- [6] A. Sakai, S. Minami, T. Koretsune, T. Chen, T. Higo, Y. Wang, T. Nomoto, M. Hirayama, S. Miwa, D. N. Hamane, F. Ishii, R. Arita, and S. Nakatsuji, Nature **581**, 53 (2020).
- [7] A. Sakai, Y. P. Mizuta, A. A. Nugroho, R. Sihombing, T. Koretsune, M. Suzuki, N. Takemori, R. Ishii, D. N. Hamane, R. Arita, P. Goswami, and S. Nakatsuji, Nature Physics **14**, 1119 (2018).
- [8] S. N. Guin, K. Manna, J. Noky, S. J. Watzman, C. Fu, N. Kumar, W. Schnelle, C. Shekhar, Y. Sun, J. Gooth, and C. Felser, NPG Asia Mater. **11**, 16 (2019).
- [9] K. Sumida, Y. Sakuraba, K. Masuda, T. Kono, M. Kakoki, K. Goto, W. Zhou, K. Miyamoto, Y.

Miura, T. Okuda & A. Kimura, Comms. Mater. **1**, 89 (2020)

- [10] Y. Sakuraba, K. Hyodo, A. Sakuma, and S. Mitani, Phys. Rev. B **101**, 134407 (2020).
- [11] M. Ikhlas, T. Tomita, T. Koretsune, M. Suzuki, D. N. Hamane, R. Arita, Y. Otani, and S. Nakatsuji, Nature Physics **13**, 1085 (2017).
- [12] W. J. Takei, G. Shirane, and B. C. Frazer, Phys. Rev. **119**, 1893 (1960).
- [13] W. J. Takei, R. R. Heikes, and G. Shirane, Phys. Rev. **125**, 1893 (1962).
- [14] S. Nakagawa and M. Naoe, J. Appl. Phys. **75**, 6568 (1994).
- [15] K. M. Ching, W. D. Chang, T. S. Chin, J. G. Duh, and H. C. Ku, J. Appl. Phys. **76**, 6582 (1994).
- [16] Y. Yasutomi, K. Ito, T. Sanai, K. Toko, and T. Suemasu, J. Appl. Phys. **115**, 17A935 (2014).
- [17] K. Kabara, and M. Tsunoda, J. Appl. Phys. **117**, 17B512 (2015).
- [18] K. Ito, Y. Yasutomi, K. Kabara, T. Gushi, S. Higashikozono, K. Toko, M. Tsunoda, and T. Suemasu, AIP Advances **6**, 056201 (2016).
- [19] S. Isogami, K. Masuda, and Y. Miura, Phys. Rev. Mater. **4**, 014406 (2020).
- [20] X. Shen, A. Chikamatsu, K. Shigematsu, Y. Hirose, T. Fukumura, and T. Hasegawa, Appl.

Phys. Lett. **105**, 072410 (2014).

[21] H. Nakayama, K. Masuda, J. Wang, A. Miura, K. Uchida, M. Murata, and Y. Sakuraba, Phys. Rev. Mater. **3**, 114412 (2019).

[22] P. Blaha, K. Schwarz, G. K. H. Madsen, D. Kvasnicka, J. Luitz, R. Laskowski, F. Tran, L. D. Marks, <http://www.wien2k.at>.

[23] S. Isogami, A. Anzai, T. Gushi, T. Komori, and T. Suemasu, Jpn. J. Appl. Phys. **57**, 120305 (2018).

[24] K. Hasegawa, M. Mizuguchi, Y. Sakuraba, T. Kamada, T. Kojima, T. Kubota, S. Mizukami, T. Miyazaki, and K. Takanashi, Appl. Phys. Lett. **106**, 252405 (2015).

[25] K. Kabara, M. Tsunoda, and S. Kokado, AIP Advances **7**, 056416 (2017).

[26] Y. Hirokane, Y. Tomioka, Y. Imai, A. Maeda, and Y. Onose, Phys. Rev. B **93**, 014436 (2016).

[27] T. Miyasato, N. Abe, T. Fujii, A. Asamitsu, S. Onoda, Y. Onose, N. Nagaosa, and Y. Tokura, Phys. Rev. Lett. **99**, 086602 (2007).

[28] J. Weischenberg, F. Freimuth, S. Blugel, and Y. Mokrousov, Phys. Rev. B **87**, 060406 (2013).

[29] M. Meng, S. X. Wu, L. Z. Ren, W. Q. Zhou, Y. J. Wang, G. L. Wang, and S. W. Li, *Appl. Phys. Lett.* **106**, 032407 (2015).

[30] S. Onoda, N. Sugimoto, and N. Nagaosa, *Phys. Rev. B* **77**, 165103 (2008).

[31] T. Komori, T. Gushi, A. Anzai, L. Vila, J. P. Attané, S. Pizzini, J. Vogel, S. Isogami, K. Toko, and T. Suemasu, *J. Appl. Phys.* **125**, 213902 (2019).

[32] A. Miura, K. Masuda, T. Hirai, R. Iguchi, T. Seki, Y. Miura, H. Tsuchiura, K. Takanashi, and K. Uchida, *Appl. Phys. Lett.* **117**, 082408 (2020).

[33] S. Isogami, K. Takanashi, and M. Mizuguchi, *Appl. Phys. Express* **10**, 073005 (2017).

## <Figure captions>

**Figure 1.** Measurement configuration of anomalous Nernst voltage ( $V_{ANE}$ ) and anomalous Hall voltage ( $V_{AHE}$ ) for the MgO substrate / Mn<sub>4</sub>N (20 nm) / Al (2 nm). The right schematic illustration represents the crystal structure of the Mn<sub>4</sub>N unit cell and magnetic structures type-A and -B.

**Figure 2.** (a,b) Out-of-plane X-ray diffraction profiles of sample-I and -II. The red and blue lines indicate the peak fitting to evaluate the degree of order of nitrogen ( $S$ ). (c,d) Magnetization curves of sample-I and -II.

**Figure 3.** (a) Representative anomalous Hall resistivity ( $\rho_{xy}$ ) as a function of applied magnetic field along  $z$ -direction ( $H_z$ ) at 300 K. (b, c, d) Dependence of anomalous Hall resistivity ( $\rho_{xy}$ ) (b), longitudinal resistivity ( $\rho_{xx}$ ) (c), and anomalous Hall conductivity ( $\sigma_{xy}$ ) (c) on measurement temperature ( $T$ ).

**Figure 4.** (a) Representative anomalous Nernst voltage ( $V_{ANE}$ ) at 300 K as a function of applied magnetic field pointing in the  $z$ -direction ( $H_z$ ). The inset represents saturated  $V_{ANE}$  as a function of temperature gradient ( $\nabla T_x$ ). The solid line shows the least-squares fitting with linear function, of which the slope gives  $V_{ANE}/(w \cdot \nabla T_x)$ . (b) Thermoelectric power ( $S_{ANE}$ ) for various materials plotted against

saturation magnetization ( $\mu_0 M_s$ ). The red color represents the target values for heat flux sensors.

**Figure 5.** (a,b) Calculated anomalous Hall conductivity ( $\sigma_{xy}$ ) (a) and transverse thermoelectric coefficient ( $\alpha_{xy}$ ) (b) as a function of chemical potential ( $\mu$ ) for the Mn<sub>4</sub>N unit cell. The dashed and solid lines represent the results for magnetic structure type-A and -B, respectively.

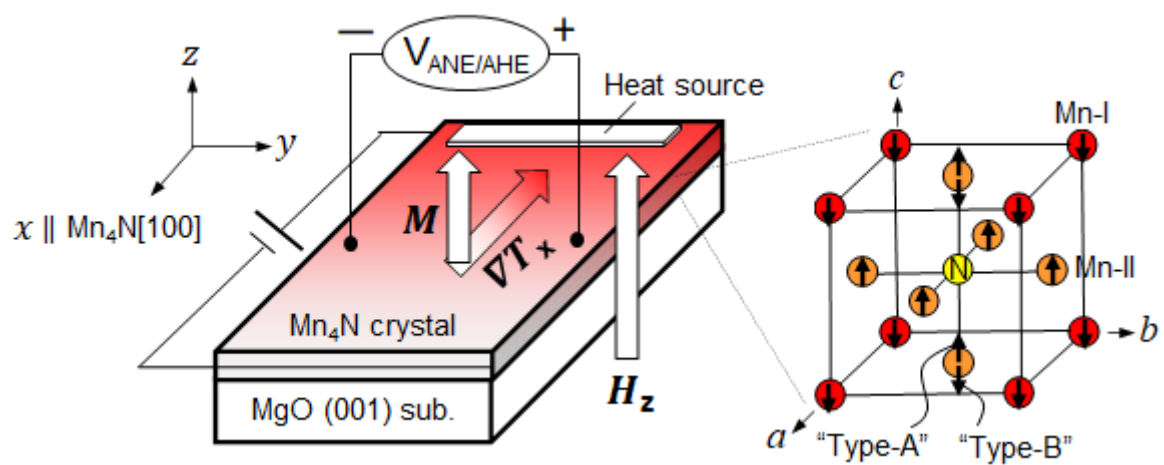


Fig. 1

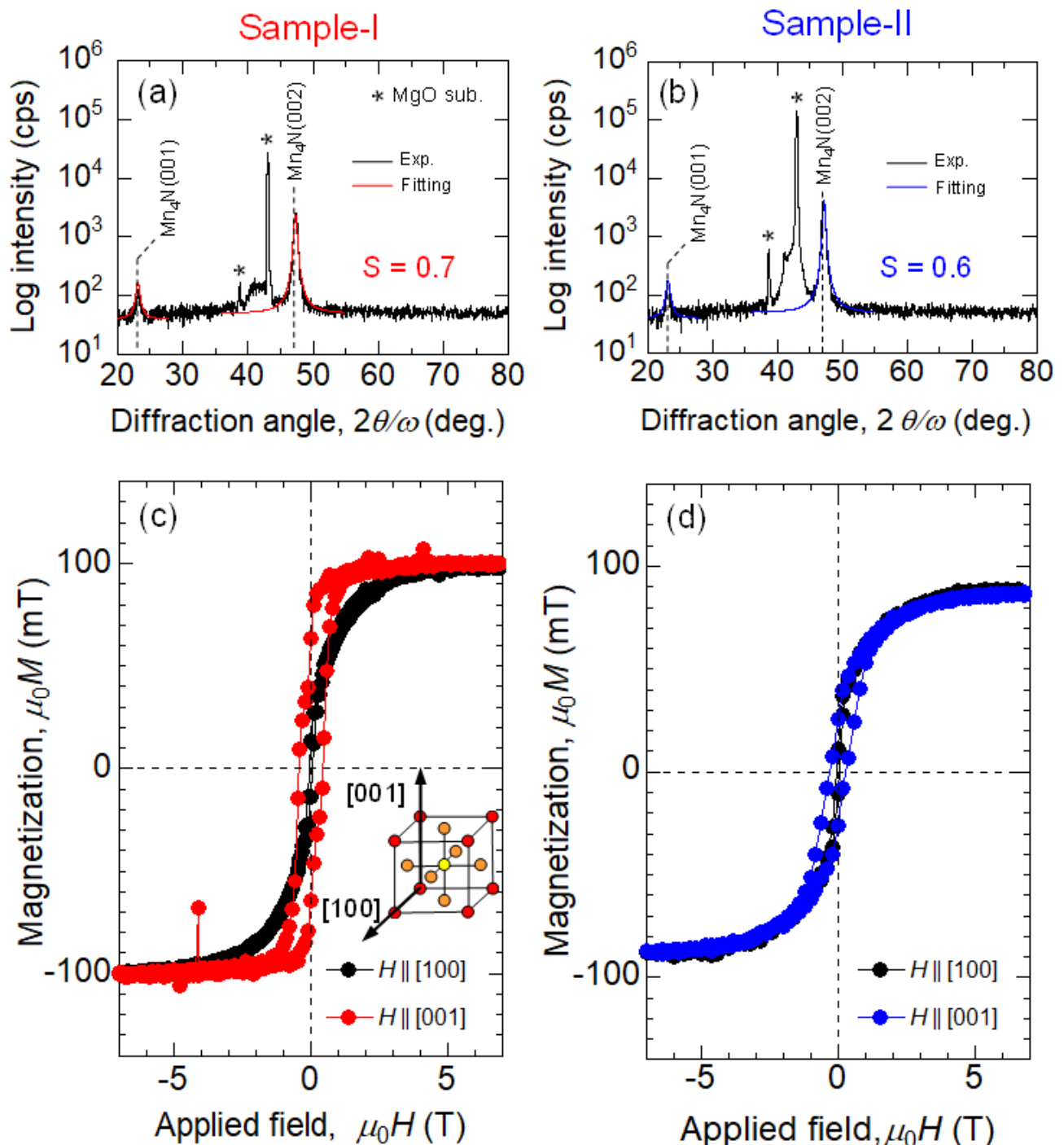


Fig. 2

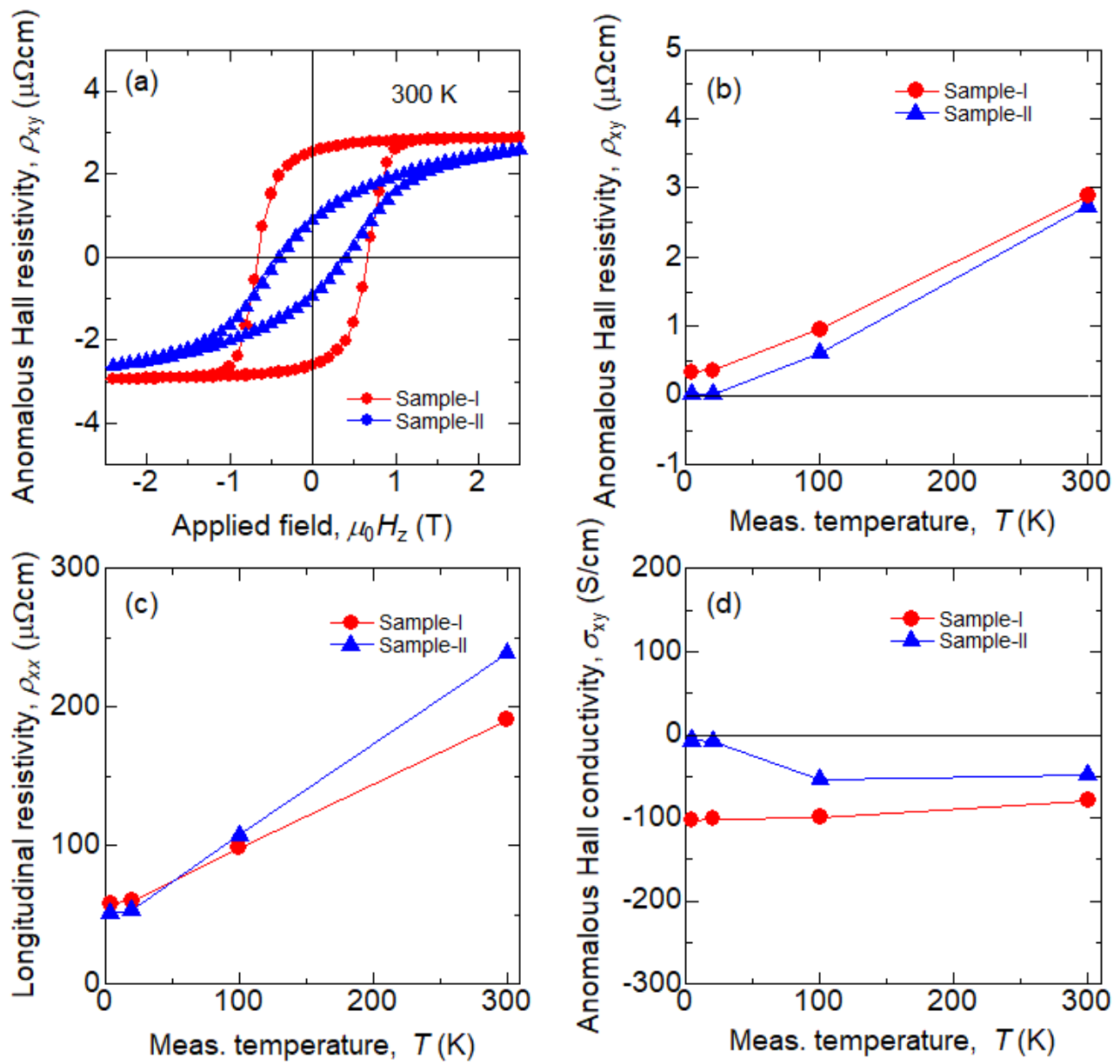


Fig. 3

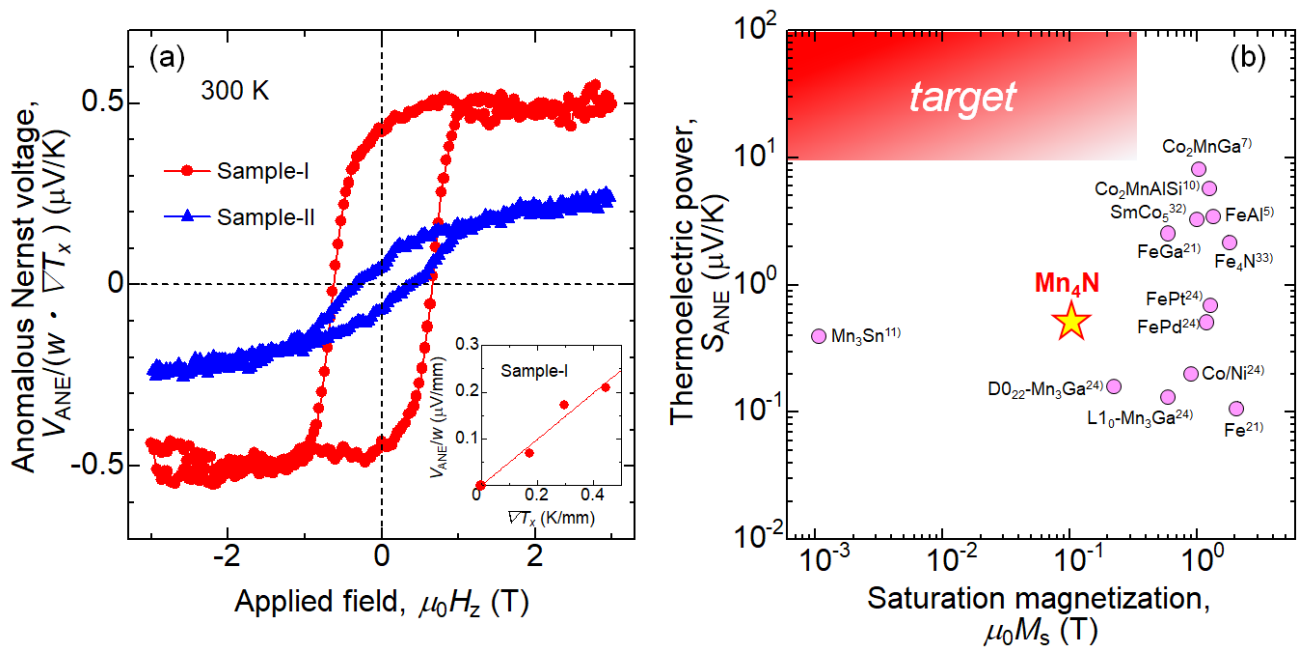


Fig. 4

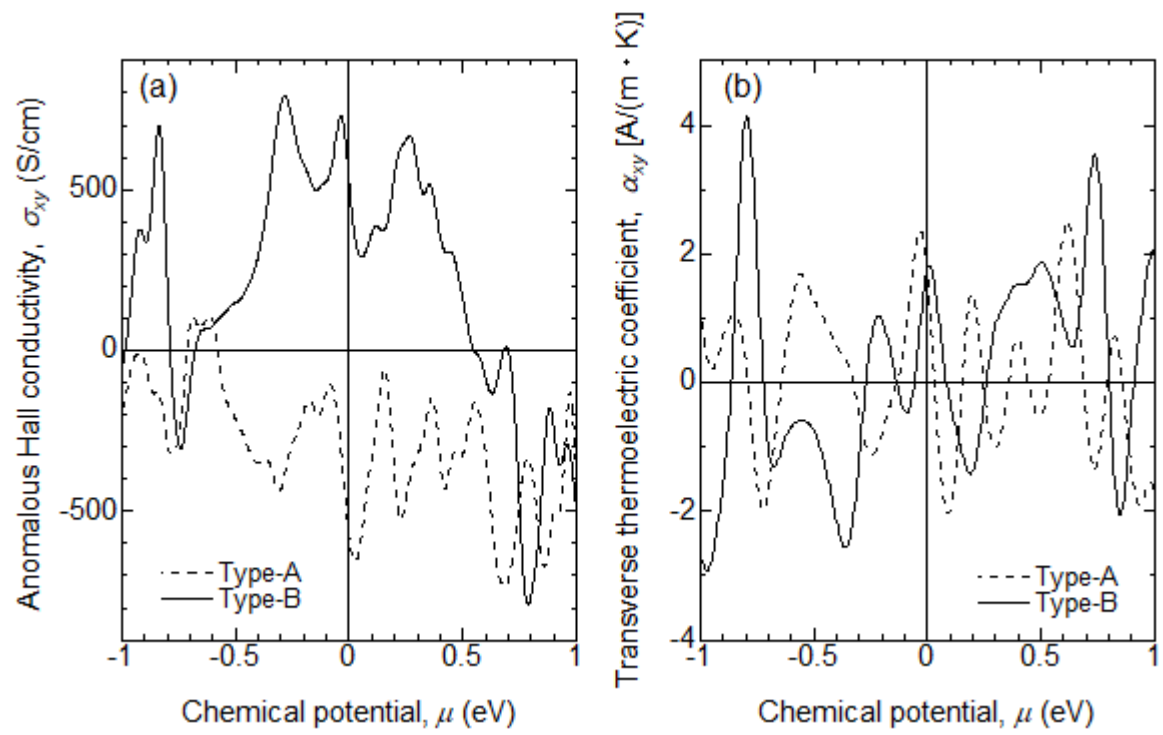


Fig. 5